JOURNAL OF GEOPHYSICAL RESEARCH, VOL. 114, A07204, doi:10.1029/2008JA013955, 2009

Formation of the Harang reversal and its dependence on plasma sheet conditions: Rice convection model simulations

Matina Gkioulidou,[1] Chih-Ping Wang,[1] Larry R. Lyons,[1] and Richard A. Wolf[2]

Received 29 November 2008; revised 3 February 2009; accepted 19 March 2009; published 2 July 2009.

[1] The goal of this paper is to understand the formation of the Harang reversal and its association with the region 2 field-aligned current (FAC) system, which couples the plasma sheet transport to the ionosphere. We have run simulations with the Rice convection model (RCM) using the Tsyganenko 96 magnetic field model and realistic plasma sheet particle boundary conditions on the basis of Geotail observations. Our results show that the existence of an overlap in magnetic local time (MLT) of the region 2 upward and downward FAC is necessary for the formation of the Harang reversal. In the overlap region the downward FAC, which is located at lower latitudes, is associated with low-energy ions that penetrate closer to Earth toward the dawn side, while the upward FAC, which is located at higher latitudes, is associated with high-energy ions. Under the same enhanced convection we compare the Harang reversal resulting from a hotter and more tenuous plasma sheet with the one resulting from a colder and denser plasma sheet. For the former case the shielding of the convection electric field is less efficient than for the latter case, allowing low-energy protons to penetrate further earthward, resulting in a Harang reversal that extends to lower latitudes, expands wider in MLT, and is located further equatorward than the upward FAC peak and the conductivity peak. The return flows of the Harang reversal in the hot and tenuous case are located in a low conductivity region. This leads to an enhancement of these westward flows, resulting in subauroral polarization streams (SAPS).

Citation: Gkioulidou, M., C.-P. Wang, L. R. Lyons, and R. A. Wolf (2009), Formation of the Harang reversal and its dependence on plasma sheet conditions: Rice convection model simulations, *J. Geophys. Res.*, *114*, A07204, doi:10.1029/2008JA013955.

1. Introduction

[2] The Harang reversal is a region of converging electric fields in the nightside ionosphere at auroral latitudes. *Harang* [1946] originally referred to this phenomenon, using magnetometer data, as a discontinuity where the westward and eastward electrojets overlap in local time. However, we prefer to use the term "reversal" for it, since it involves the rotation of electric field vectors from south to north rather than a physical discontinuity.

[3] Latitudinally, across the Harang reversal, $\mathbf{E} \times \mathbf{B}$ convection flow reverses its direction from eastward, at higher latitudes, to westward, at lower latitudes. Observations of these ionospheric flows, using radar data, have shown dependence of the reversal's position on geomagnetic activity. More specifically, it moves equatorward when *Kp* increases [e.g., *Nielsen and Greenwald*, 1979], and to earlier (later) MLT when IMF By becomes more positive in the Northern (Southern) Hemisphere [*Rodger et al.*, 1984].

[4] The Harang reversal is located near the inner edge of plasma sheet and is closely related to the region 2 FAC [*Zou et al.*, 2009]. Moreover, recent larger-scale analyses, also of radar data [*Bristow and Jensen*, 2007; *Zou et al.*, 2009], have firmly shown a relationship between the evolution of the Harang reversal and the substorm onset. This last feature reveals the importance of the Harang reversal, since the substorm onset mechanism is still under debate and has been theoretically predicted to be related with the reversal [*Lyons et al.*, 2003].

[5] *Erickson et al.* [1991], using the Rice convection model (RCM) simulations with simplified MLT-dependent boundary conditions having the number of hot ions reduced on the dawn side, gave a theoretical explanation for the formation of the Harang reversal. They described it as the result of the dawnside depletion of hot ions owing to their duskward magnetic drift motion in addition to the absence of energetic ions source from the dawnside low-latitude boundary layer. This depletion causes upward region 2 FAC to flow from the ionosphere to the plasma sheet. Current continuity in the ionosphere requires convergence of Pedersen currents, and therefore the formation of converging electric fields in the same region. This results in the reversal of the north–south electric field component forming the Harang reversal. However, since pressure and the associated distributions of the region 2 FAC are contributed mostly by plasma sheet ions and conductivity depends mostly on plasma sheet electrons, boundary conditions that can represent the plasma sheet with realistic MLT dependence are

[1]Department of Atmospheric and Oceanic Sciences, University of California, Los Angeles, California, USA.
[2]Physics and Astronomy Department, Rice University, Houston, Texas, USA.

0148-0227/09/2008JA013955$09.00

important for quantitatively investigating the formation of the Harang reversal.

[6] In this paper we evaluate the underlying physical processes of the Harang reversal and determine how the plasma sheet, under different solar wind and IMF conditions, affects the formation and characteristics of the Harang reversal. We use the RCM with realistic plasma sheet boundary conditions on the basis of a statistical study of 11-year Geotail data for 16 different interplanetary conditions. In section 3, we show that the dawnside energetic ion depletion effect described by *Erickson et al.* [1991] is by itself not enough; instead, an overlap in the midnight to dawn region of the downward (located at lower latitudes) and upward (located at higher latitudes) region 2 currents in the midnight to dawn region, owing to different drift paths of low- and high-energy particles [*Harel et al.*, 1981b], is necessary. In section 4, we quantitatively characterize the Harang reversal in terms of its MLT and latitudinal extent, as well as in terms of return westward flow in the Harang reversal. We determine the correlation between these properties and our boundary conditions and provide a physical explanation for this correlation. We also show that the auroral conductance, which depends on the plasma sheet electrons, plays an important role in the formation and characteristics of the Harang reversal.

2. Rice Convection Model

2.1. Plasma Transport and Distributions

[7] Our study requires a model that can appropriately describe the drift transport physics in the near-Earth magnetosphere and the coupling with the ionosphere self-consistently. The RCM [*Harel et al.*, 1981a; *Toffoletto et al.*, 2003] simulates the electric and magnetic drift of ions and electrons and their electrodynamic coupling to ionosphere. More specifically, it calculates the bounce–averaged electric drift and magnetic drift of a flux tube filled with an isotropic distribution of ions or electrons at specified kinetic energies inside the closed field line region of the magnetosphere. In slow flow, a particle's total energy $E_K + q\Phi$ is conserved as it drifts, where E_K is the particle's kinetic energy, Φ is the electric potential, and q is the particle's electric charge. For an isotropic particle distribution, which is a good approximation in the plasma sheet [*Stiles et al.*, 1978; *Nakamura et al.*, 1991], the particle kinetic energy change can be simply determined by the change in flux tube volume according to the relation $E_k = \lambda \mathrm{V}^{-2/3}$ [*Wolf*, 1983], where λ is constant along a particle's drift path and is called the energy invariant and V is the flux tube volume

$$\mathsf{V} = \int_{sh}^{nh} \frac{ds}{B(\vec{x}, t)} \tag{1}$$

where *nh* and *sh* refer to the Northern and Southern Hemisphere endpoints of the field line in the ionosphere.

[8] For an isotropic particle distribution the bounce-averaged drift velocity $\mathbf{V}_\mathrm{D}$ of particles of a given λ at position $\mathbf{x}$ and time t is independent of its pitch angle and can therefore be described as [*Wolf*, 1983],

$$\mathbf{V}_\mathrm{D}(\mathbf{x}, t) = \frac{\mathbf{B}(\mathbf{x}, t) \times \nabla\Phi(\mathbf{x}, t)}{|\mathrm{B}(\mathbf{x}, t)|^2} + \frac{\mathbf{B}(\mathbf{x}, t) \times \lambda \nabla \mathsf{V}(\mathbf{x}, t)^{-2/3}/q}{|\mathrm{B}(\mathbf{x}, t)|^2} \tag{2}$$

The first term on the right side of (2) is the electric drift and the second term is the magnetic drift. The RCM traces the drift trajectory of particles of different λ within a flux tube using (2) with given $\Phi(\mathbf{x}, t)$ and $\mathrm{V}(\mathbf{x}, t)$. The RCM grid is specified in the ionosphere, so $\mathbf{B}$ in equation (2) is the magnetic field in the ionosphere. The RCM solves for $\Phi(\mathbf{x}, t)$ self-consistently with plasma distributions. A 3-D distribution of magnetic fields in the magnetosphere is required for computing V and for mapping from the ionosphere to the plasma sheet. The magnetic field that we use in our simulations is the Tsyganenko 96 magnetic field model (T96) [*Tsyganenko*, 1995, 1996]. The T96 model is capable of providing a realistic large-scale magnetic field configuration within the region from our outer boundary locations ($r \sim 20$ RE) to the inner magnetosphere. Therefore, it provides reasonable mapping between the ionosphere and magnetosphere. However, the T96 has limitations for our purposes, including the dawn-dusk symmetry of the magnetic field and that it is not in force balance with the RCM plasma pressure.

[9] In the RCM, particle fluxes are modeled by dividing the energy spectrum into several energy channels (30 channels for electrons and 85 for protons in this study) and by approximating the plasma differential flux within each energy channel by $j(E_K) = j_\mathrm{i}(E_{K\mathrm{i}})$, where $E_{k\mathrm{i}}$ is the represented kinetic energy of the ith channel. The number of ith channel particles per unit magnetic flux, η_i, can be calculated from j_i, λ_i, and V, and is conserved along the drift trajectory described by equation (2) if there are no losses. Two particle species, protons and electrons are simulated in our study.

[10] Each simulation starts from a specified distribution of η_i ($\mathbf{x}$, $t = 0$) at the model boundary (boundary conditions) and within the model region (initial conditions). No initial η_i is used in our runs. At a later time t_1, particles of different λ which occupied the same flux tube at $t = 0$ will have drifted apart because of their λ-dependent drift velocities (2). Plasma loss is modeled with specified loss rates owing to charge exchange for ions and owing to pitch angle scattering for electrons (pitch angle scattering losses, even under strong diffusion, are too small to be significant for plasma sheet ions). Therefore the spatial distribution of $\eta_\mathrm{i}(\mathbf{x})$ at $t = t_1$ is obtained by tracing the trajectories of λ_i backward in time from $t = t_1$ to $t = 0$ and reducing the η_i values at $t = 0$ by the number of particle lost. The spatial distributions of plasma density n and pressure p for each species are then obtained from $\eta_\mathrm{i}(\mathbf{x}, t = t_1)$,

$$n(\mathbf{x}, t) = \sum_i \frac{\eta_i(\mathbf{x}, t)}{\mathsf{V}(\mathbf{x}, t)}, \text{ and } p(\mathbf{x}, t) = \frac{2}{3} \sum_\mathrm{i} \frac{\eta_i(\mathbf{x}, t)}{\mathsf{V}(\mathbf{x}, t)} \lambda_\mathrm{i} \mathsf{V}(\mathbf{x}, t)^{-2/3} \tag{3}$$

Temperature T can be obtained from p/nk_B where k_B is Boltzmann's constant.

2.2. Self-Consistent Electric Field

[11] In the magnetosphere, a pressure gradient perpendicular to $\nabla\mathsf{V}$ causes a divergence or convergence of perpendicular currents. Since current continuity must be satisfied, field-aligned currents flow into or out of ionosphere. Using the plasma pressure and flux tube volume, the field-aligned

current can be computed according to the Vasyliunas equation [*Vasyliunas*, 1970],

$$j_{\parallel} = \frac{B_i \hat{b}}{2B_e} \cdot \nabla \mathsf{V} \times \nabla p \quad (4)$$

where $j_{\parallel}$ is the ionospheric field-aligned current density of the Northern or Southern Hemisphere (north-south symmetry is assumed). If $\nabla \mathsf{V}$ is radial, it is clear that a westward (eastward) pressure gradient results in upward (downward) field-aligned currents flowing out of (into) ionosphere. The self-consistent electric field is obtained by satisfying current continuity in the ionosphere as well,

$$\nabla_i \cdot \left[\overleftrightarrow{\sum} \cdot (\nabla_i \Phi_i) \right] = -j_{\parallel} \sin(I) = -\frac{B_i}{2B} \hat{b} \cdot \nabla \mathsf{V} \times \nabla p \sin(I) \quad (5)$$

where $\overleftrightarrow{\sum}$ is the field-line integrated conductivity tensor owing to both hemispheres, I is the dip angle of the magnetic field in the ionosphere. Subscript i refers to ionosphere-computed quantities.

[12] With given $\overleftrightarrow{\sum}$ and boundary conditions at the high- and low-latitude boundary, (5) can be solved to obtain Φ_i. The conductivity tensor $\overleftrightarrow{\sum}$ includes both the Hall and Pedersen conductivities. The conductance includes solar-EUV-generated conductance that is estimated from the IRI-90 empirical ionosphere driven by F10.7 and the *Ap* index, and auroral conductance, which, in this study, is estimated using the electron precipitation from the simulated plasma distributions, assuming 1/3 of strong pitch angle scattering and the algorithm of *Robinson et al.* [1987]. Conductance change associated with the region 1 FAC is not included. The electron precipitation rate is currently assumed to be local time–independent. The high-latitude boundary condition for the potential is a Dirichlet boundary condition; the overall strength of convection is determined by setting the total range of potential on the boundary equal to the polar cap potential $\Delta\Phi_{PC}$. A two-cell convection pattern is assigned to describe the electric potential inside the polar cap. A phase shift is used to describe the rotation of the separation line of the two convection cells relative to the noon-midnight meridian (1 hour MLT westward rotation is used in this run). The low-latitude boundary condition incorporates the effects of the equatorial electrojet. Note that the RCM includes the contribution to the electric field in the magnetospheric equatorial plane from the induced electric field when time-changing magnetic fields are used for the mapping. Using the Φ solved at each time step, particles are moved to obtain the particle distributions for the next time step, thus completing one circuit around the RCM time loop.

2.3. Particle Boundary Conditions

[13] The location of the outer (poleward) boundary is specified as a circle in the equatorial plane that reaches $X \sim -20\ R_E$ at midnight and $|Y| \sim 15\ R_E$ at dawn and dusk (the center of the circle is at $X = -5\ R_E$ and $Y = 0$). The inner (equatorward) boundary is specified in the ionosphere at the 10° latitude circle. Along the outer boundary, the proton and electron distributions at different MLT are established from a fitting of two-component kappa distributions, which are a combination of one cold and one hot population, to statistical results from 11 years of Geotail observations. Statistical study of these data has already been done for northward IMF conditions [*Wang et al.*, 2007]. In this paper we extend the study to obtain the statistical results under southward IMF, which are needed for our boundary conditions. The Geotail results are binned into 16 different interplanetary conditions, each being a combination of three interplanetary parameters: solar wind number density (N_{sw}), solar wind speed (V_{sw}), and the magnitude of the northward (8 cases) or southward (8 cases) IMF B_z ($|B_{z,IMF}|$), each of them being divided into a low- and high-energy range. This gives 16 different MLT-dependent boundary conditions that realistically represent the plasma sheet conditions observed corresponding to a variety of interplanetary conditions. The two-component kappa distribution we use is shown in equation (A1). The ranges, averages, and standard deviations of the solar wind parameters for each one of the 16 cases are listed in Table A1, while the parameters used for the cold and hot population for each one of the 16 cases are listed in Table A2 (northward IMF cases) and Table A3 (southward IMF cases); see also Appendix A.

3. Physics of Harang Reversal Formation

[14] We first use the RCM results to examine what are the physical processes that result in the reversal of electric fields in the region of the Harang reversal.

[15] We ran the simulation with constant cross polar cap potential drop ($\Delta\Phi_{PCP}$) = 30 kV, IMF B_z = 0 and *Dst* = −10 nT (IMF B_z and D_{st} are used as an input for the T96) for 5 simulation hours, and then step increased $\Delta\Phi_{PCP}$ to 100 kV and decreased IMF B_z to −7 nT and *Dst* to −11 nT at t = 0 and kept them constant for another 5 hours (two other inputs, Pdyn = 1.7 nPa and IMF B_y = 0, for the T96, are kept constant throughout the simulation). Since the T96 magnetic field is not in force balance with the simulated plasma pressure, we chose the above values for the T96 parameters in order to give typical magnetic field configurations for weak and for enhanced convection conditions. Our plasma boundary conditions are those of case 5N (see Table A2) and are kept constant throughout the simulation.

[16] In Figure 1 we show equatorial plasma pressure and ionospheric FAC (color contours; negative for upward FAC from and positive for downward to ionosphere) and equipotentials (contours) projected to the equatorial plane, for times t = 4 min, 8 min, 20 min, and 1 hour after the increase of the polar cap potential drop. We also show the ionospheric FAC and equipotentials in the ionosphere for the same times. The Harang reversal, identified by a heavy dashed line, starts to form ∼20 min after convection is enhanced (t = 20 min) and becomes well developed at t = 1 hour.

[17] At t = 4 min, a pressure peak is located on the dusk side, owing to the duskward magnetic drift of high-energy protons. Once a pressure peak is developed, there are both westward and eastward pressure gradients and thus an upward and downward FAC pair is formed, according to equation (4). We consider only the azimuthal pressure gradient, because the flux tube volume gradient is mainly in the radial direction. Near midnight, this FAC pair can be seen at $X \sim -7$ to $-10\ R_E$ in the equatorial plane and at

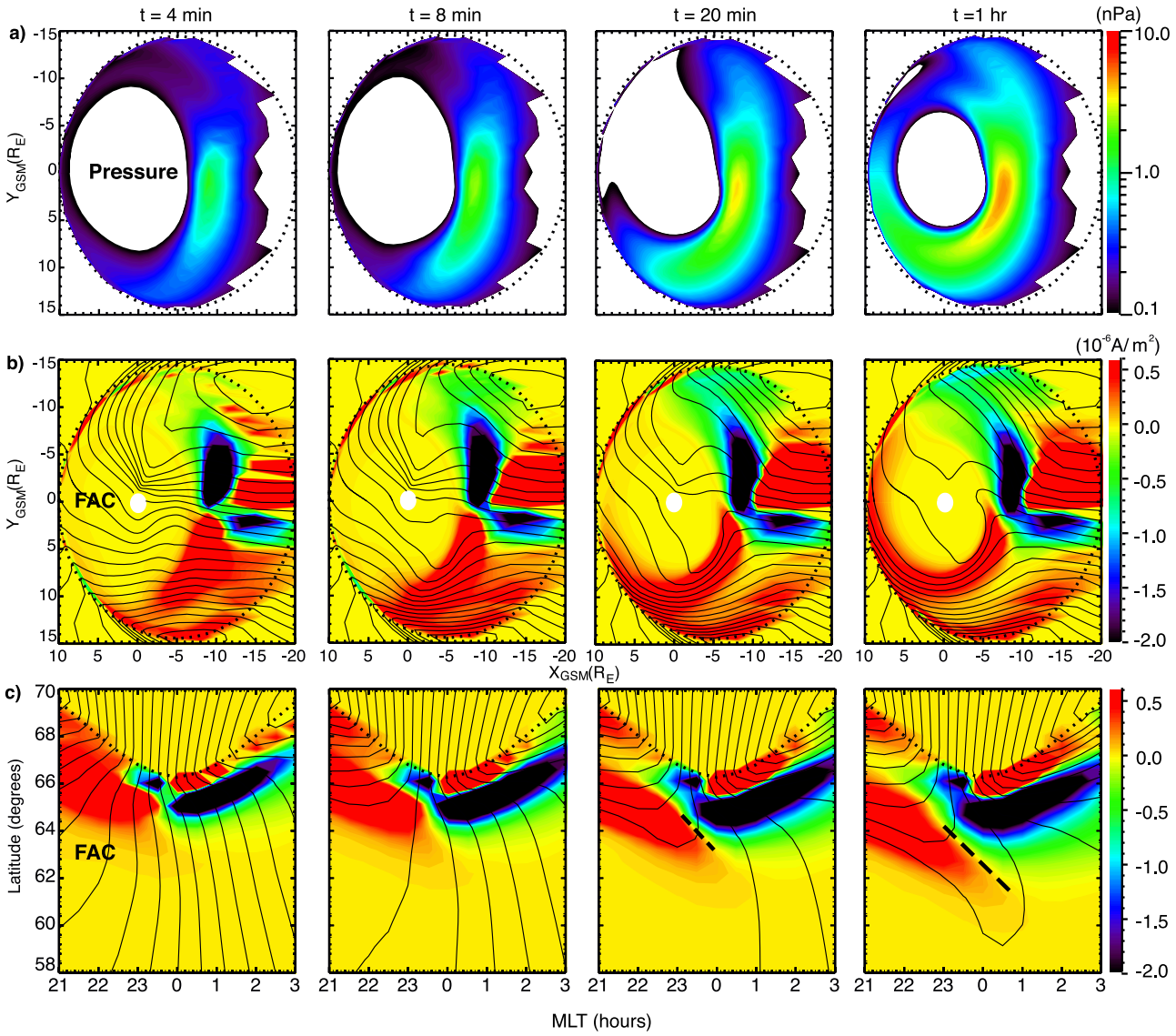

Figure 1. (a) Total plasma pressure in nPa at the equatorial plane. (b) Ionospheric field-aligned currents (color contour, negative values for upward current from, and positive for downward to the ionosphere) and equipotentials (contours with 5 kV interval) mapped to the equatorial plane (the corotation electric field is not included in these plots). (c) Same as Figure 1b, but in the ionosphere with 1 kV contour interval, for time t = 4 min, 8 min, 20 min, and 1 hour after the increase of the potential drop. The equipotential pattern throughout the paper does not include the corotation electric field. Dotted black lines represent our outer boundary location. The heavy dashed lines indicates roughly the location of the Harang reversal.

$\sim$65° latitude in the ionosphere. There is another FAC pair located near midnight at higher latitudes (downward post-midnight, upward premidnight) resulting from our boundary conditions, which have a pressure minimum at midnight. They are actually part of the region 1 currents that extend into the RCM modeling region, though their structure depends substantially on the particle boundary conditions applied. This high-latitude pair is not the focus of this study. At this early time, the electric field is only weakly shielded from the region earthward of the plasma sheet. By t = 8 min, particles drift further earthward leading to pressure gradients closer to the Earth and the FAC regions expand equatorward and azimuthally. This strengthens the shielding of the convection electric field from the near-Earth region. The shielding effect will be discussed in more detail in section 4. At even later times (t = 20 min, t = 1 hour), the shielding is almost fully developed and the formation of the Harang reversal is apparent. Note that when the Harang reversal is formed at t = 20 min, there is a premidnight region of MLT overlap at $\sim$62–64° latitude between the duskside region of substantial ($\sim 0.5 \times 10^{-6}$ A/m^2) downward FAC and the dawnside region of upward FAC, an overlap which does not occur at the earlier times.

[18] We next address the following two questions: What is responsible for the overlap of the upward and downward

region 2 FAC, and why does this overlap result in the Harang reversal?

3.1. MLT Overlap of FAC

[19] In order to understand why an overlap region of FAC is created, we need to determine the relative contributions to the FAC from different energy particles in this region. In Figure 2 (left) we show pressure and the corresponding FAC caused by low-energy (30–420 eV at boundary location: X ~ −20 R_E at midnight) protons and high-energy (420–13 keV at the same boundary location) protons, as well as the total FAC contributed by protons of all energies, for time t = 4 min when there is no Harang reversal. In Figure 2 (right) we show the same quantities for t = 5 hours when the Harang reversal is well developed. Owing to the energy-dependent magnetic drift, which is different for electrons (dawnward) and protons (duskward), the electron and low-energy proton inner edge is located closer to the Earth on the dawn side, while the high-energy proton inner edge is located closer to the Earth on the dusk side. The closer to the Earth particles penetrate, the more they get energized. As a result, the pressure for electrons and the low-energy protons peaks at midnight toward the dawn side, while the high-energy proton pressure peak extends toward the dusk side. Each of these pressure peaks is associated with a downward and upward FAC pair. Notice the different positions of the centers of these FAC pairs. The boundary between the upward and downward FAC for the low-energy protons is located postmidnight while the boundary for the high-energy protons is located premidnight.

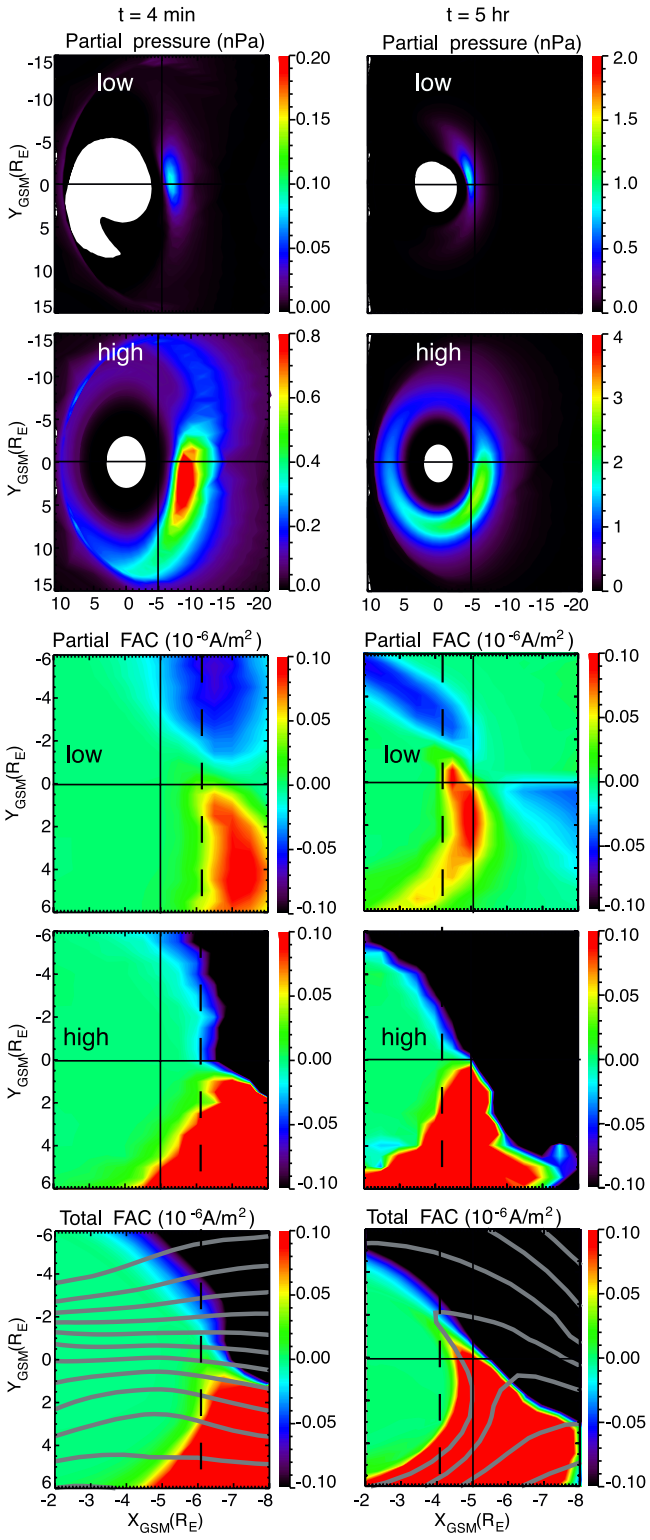

[20] At the earlier time t = 4 min, the peaks of both low- and high-energy particle pressures, and therefore their corresponding FAC pair, are at the same distance from the Earth. This means that the total FAC has no overlap in MLT between the downward and upward FAC and the Harang reversal is not seen. At time t = 5 hours, the low-energy protons, following the electric drift, are able to penetrate further earthward, while the high-energy protons, which are more strongly affected by the magnetic drift, remain further away. This causes the dawn side pressure peak of the low-energy population as well as its associated FAC pair to be located closer to the Earth than for the high-energy population.

[21] Therefore, when the Harang reversal is formed, the region 2 FAC has an overlap region. The downward FAC associated with low-energy protons extends to the same near midnight MLT as does the upward FAC associated with high-energy protons, but the downward FAC lies closer to the Earth, that is, at lower latitudes in the ionosphere.

3.2. Electric Field Response to FAC Changes

[22] Having demonstrated the cause of the FAC overlap region, we now investigate how the electric field perturbations caused by the changes of the FAC result in the reversal of the total electric field.

[23] We look at changes that occur during two time intervals: (1) t_1 = 4 min to t_2 = 8 min and (2) t_1 = 20 min

Figure 2. From top to bottom: pressure caused by low-energy protons (30–420 eV at the boundary x = 20 R_E and y = 0), pressure caused by high-energy protons (420–13 keV at the boundary), ionospheric FAC associated with low-energy protons, ionospheric FAC associated with high-energy protons, and total ionospheric FAC (color contour) with equipotentials (contours) at equatorial plane for time t = 4 min (left column) and t = 5 hours (right column). The dashed line in the FAC panels shows the inner edge of the downward FAC caused by the low-energy protons around the midnight and dawn side.

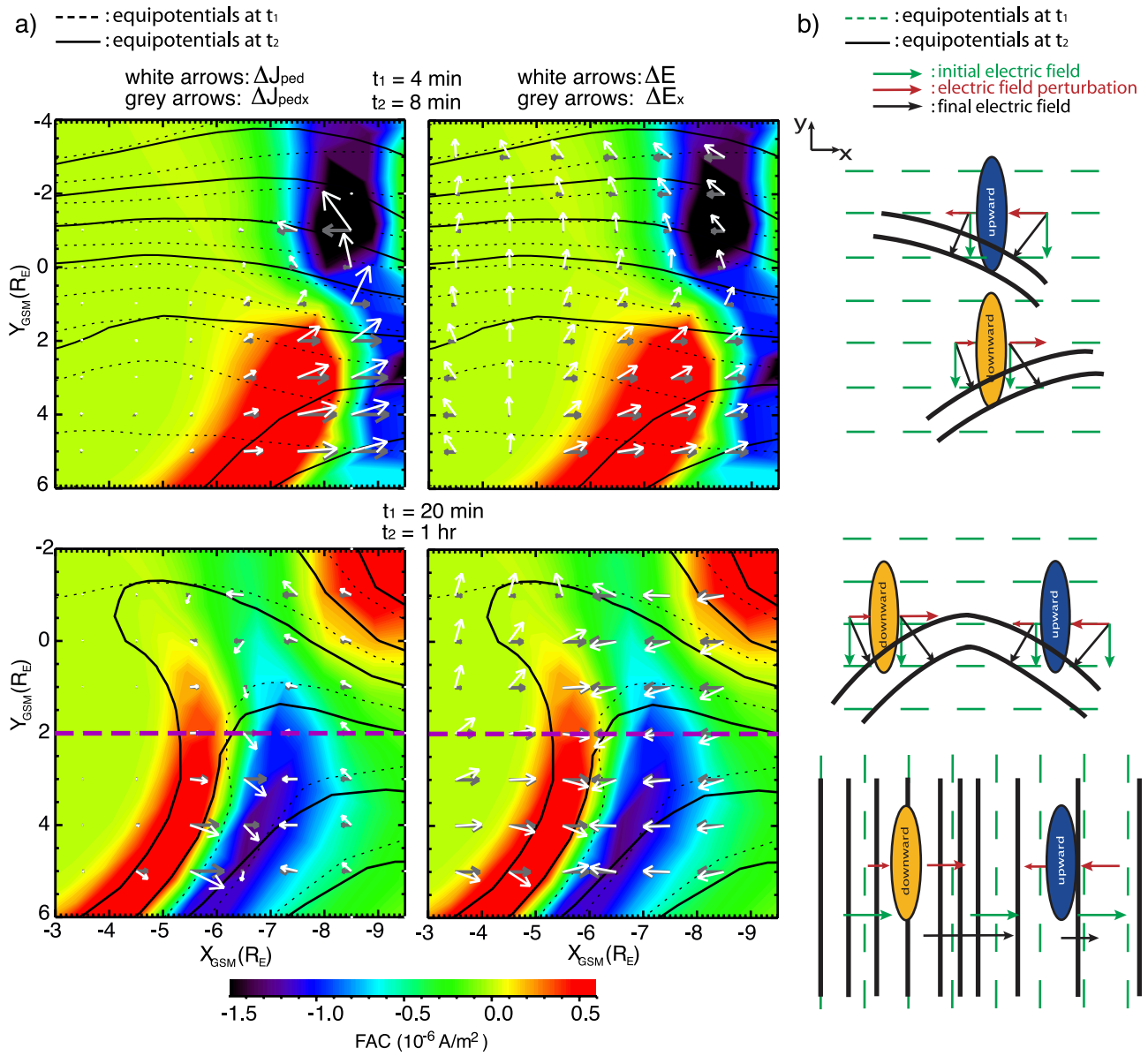

Figure 3. (a) (top) Total vector and x component of Pedersen current perturbation, unit vector and x component of the total electric field perturbation, for the time interval t_2 = 8 min to t_1 = 4 min. (bottom) The same as Figure 3a (top) but for the time interval t_2 = 1 hour to t_1 = 20 min. In all of the panels the color contour shows the FAC change $\Delta J_{//}$ and the contours represent the equipotentials for t_1 (dotted line) and t_2 (solid line). (b) Simple cartoon showing initial electric field (green arrows), the FAC change $\Delta J_{//}$, the associated *x* component of the electric field perturbations (red arrows), as well as the final electric field (black arrows). The green dashed lines represent the background equipotentials at t_1, and the solid black lines represent the equipotentials with the presence of FAC at t_2. The top cartoon refers to the time interval t_2 = 8 min to t_1 = 4 min, the middle one to the time interval t_2 = 1 hour to t_1 = 20 min and the region Y_{GSM} from 2 to −1 R_E, and the bottom one to the time interval t_2 = 1 hour to t_1 = 20 min and the region Y_{GSM} from 5 to 2 R_E. All the above ionospheric quantities are projected to the equatorial plane.

to t_2 = 1 hour. Figure 3a shows for both time intervals, the FAC change $\Delta J_{//} = J_{//2} - J_{//1}$, the ionospheric Pedersen current change, $\Delta \mathbf{J_{ped}} = \mathbf{J_{ped2}} - \mathbf{J_{ped1}}$ caused by the FAC perturbation, and the direction of the electric field change $\Delta \mathbf{E} = \mathbf{E_2} - \mathbf{E_1}$ associated with the Pedersen current perturbation, as well as the equipotentials for times t_1 and t_2. All the above ionospheric properties are projected to the equatorial plane. We show these properties for the two different time intervals in order to show the electric field perturbations in situations with and without the FAC overlap region, and thus also with and without the Harang reversal.

[24] To illustrate how electric field changes lead to the reversal of north-south electric field component associated with the Harang region, we show only the direction of $\Delta \mathbf{E}$ (unit vectors), which leaves out the effects of conductivity changes. On the basis of the simulation results, Figure 3b

shows three simple illustrations of the *x* component of the electric field perturbations that lead to the formation of the Harang reversal.

[25] Let us first focus on the first time interval results shown in Figure 3a. At time t_1, 4 min after the potential drop has been increased, the penetrating electric field (dotted equipotentials) is strong. At time $t_2 = 8$ min, plasma has moved earthward, pressure gradients have built up and therefore FAC appear in the region, downward on the dusk side and upward on the dawn side (color contours). At this time, the low-energy protons have not yet moved closer to Earth than the higher-energy protons, so the two FAC regions do not overlap. Once FAC are flowing into (downward) or out of (upward) the ionosphere, divergence (in the region of downward FAC) or convergence (in the region of upward FAC) of perpendicular Pedersen currents is required to maintain current continuity in the ionosphere. These Pedersen current perturbations $\Delta\mathbf{J_{ped}}$ are shown in Figure 3. The electric field perturbations $\Delta\mathbf{E}$ associated with these Pedersen currents are also shown in Figure 3. For both of the above perturbations white arrows show the total vector and gray arrows show the x component. Notice that $\Delta\mathbf{E_x}$ is directed earthward in the region of upward FAC and tailward in the region of downward FAC. These electric field perturbations add to the electric fields at $t_1 = 4$ min. This bends the equipotentials azimuthally, so that some shielding can be seen at $t_2 = 8$ min (solid equipotentials). Notice also that the shielding in Figure 3a is stronger on the evening side than on the dawn side. Figure 3b illustrates how this perturbation $\Delta\mathbf{E_x}$ (red arrows), added to the background electric field (green arrows), results in the new electric field (black arrows).

[26] During the later time interval, the low-energy protons have moved closer to Earth than the higher-energy protons leading to an overlap region of downward and upward FAC as discussed in section 3.1. For this later time interval, we focus on the two different spatial regions separated by a purple dashed line in Figure 3a.

[27] In the first region (Y_{GSM} from 2 to -1 R_E), we recognize the Harang reversal configuration. Notice that both $\Delta\mathbf{J_{ped}}$ and the $\Delta\mathbf{E}$, which enhances the reversal of the electric fields, change direction from tailward to earthward in the region between the downward and upward FAC perturbations, and not in the region of upward FAC perturbation as inferred by *Erickson et al.* [1991]. The way the electric field perturbations in this region result in the Harang reversal is illustrated in Figure 3b.

[28] In the second region (Y_{GSM} from 5 to 2 R_E) we notice that the equipotentials at time t_1 extend along the azimuthal direction. This is because the convection electric field has been strongly shielded on the evening side during the first time interval as mentioned before. In this region, the downward FAC perturbation is actually just equatorward of the inner edge of the electron plasma sheet, and is therefore a region of low conductivity. We should mention at this point that the strong shielding results from the very large electric field perturbations in this very low conductivity region. The perturbation $\Delta\mathbf{E}$ in this part of the overlapping region, being in the same direction as in the previous region, increases the total electric field in the region of downward FAC (equipotentials are piled up) and decreases the total electric field in the region of upward FAC (equipotentials are further apart from each other) at time t_2. The increased antiearthward electric field on the evening side causes a strong westward $\mathbf{E} \times \mathbf{B}$ convection flow, which is known as SAPS and has been observed in the ionosphere [*Anderson et al.*, 1991; *Foster and Burke*, 2002]. Our results agree with the physical explanation that was given for the generation of SAPS by *Southwood and Wolf* [1978]. In section 4 we discuss more quantitatively the features of this westward flow, which we treat as part of the Harang reversal region. The electric field perturbations of this region can be seen in Figure 3b.

4. Dependence of Harang Reversal on Plasma Sheet Conditions

[29] As discussed in section 3, the physical processes that lead to the formation of the Harang reversal are strongly related to the different contributions from electrons and protons of different energies. Thus we next investigate how these physical processes are affected by the plasma sheet density and temperature, which vary significantly with the interplanetary conditions.

[30] We have run the RCM, with the 16 different MLT-dependent plasma sheet boundary conditions listed in Table A2 for northward IMF (NIMF) and in Table A3 for southward IMF (SIMF) conditions; see Appendix A. Except for the boundary conditions, all of these simulations were run the same as for the simulation described in the previous section, other than we now increase the potential drop gradually within an hour and not as a step function, and we decrease the *Dst* from -10 to -20 nT. Again we set $t = 0$ to be when the polar cap potential drop starts to increase. The boundary conditions in each run are kept time-independent. Note that although it is unrealistic to have plasma sheet corresponding to NIMF conditions when convection has been enhanced for 5 hours, the goal of this study is to investigate how the preconditioning of the plasma sheet prior to a convection enhancement affects the physical processes that lead to the formation of the Harang reversal.

[31] For the 16 different boundary conditions, we have calculated the total number density, proton and electron total temperature, and proton total pressure from our phase space density function. These boundary values at dawn (light blue), dusk (black), and midnight (red) are shown in Figure 4. The numbers along the *x* axis refer to the cases listed in Table A1 and the letters N and S refer to the NIMF and southward SIMF conditions, respectively. The cases are ordered in this plot from less dense to more dense for both SIMF and NIMF. It can be seen that the plasma sheet under NIMF conditions is generally colder and denser than under SIMF conditions.

[32] Figure 4 shows that there is a correlation between the plasma sheet number density and plasma sheet pressure. It is known that plasma sheet pressure affects the evolution of the shielding of the convection electric field [*Garner*, 2003] in the near-Earth region. However, the shielding effect also depends on conductivity, which is related to the electron temperature. Therefore, both density and temperature contribute, in different ways, to the shielding effect. The shielding of the electric field controls whether the low-energy protons will penetrate earthward enough so that the formation of the Harang reversal is possible. Among our 16 cases we pick two extreme ones, with different Harang reversal characteristics. The first one, in which the Harang

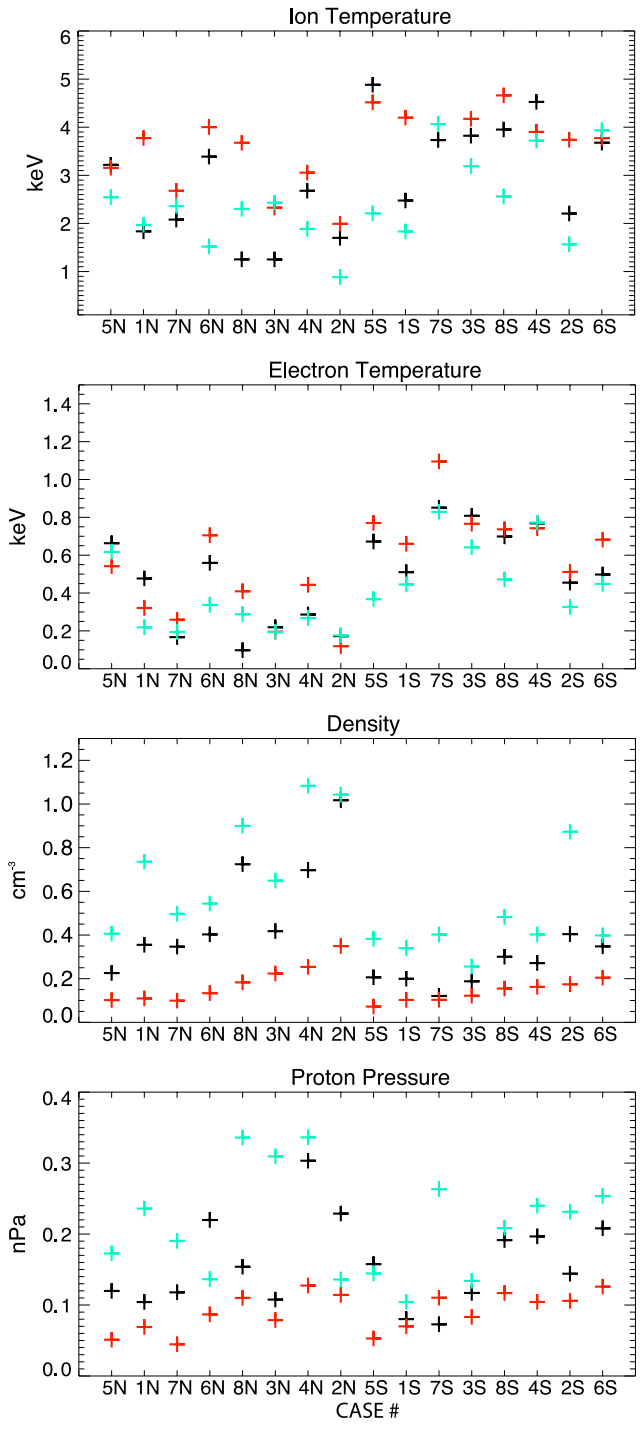

Figure 4. Ion and electron temperature, density, and pressure at the outer boundary at 0000 (red), 1800 (black), and 0600 magnetic local time (MLT) (light blue) for each of the 16 cases. The numbers refer to the cases of Table A1. The letter N (S) next to the number of each case corresponds to NIMF (SIMF) conditions.

reversal covers a very small region in MLT and latitude, is a cold and dense plasma sheet case, while the second one, in which the reversal extends to a much wider region both in MLT and latitude, is a hot and tenuous one. We investigate the reasons for this different behavior and then we show a more general correlation between the 16 plasma sheet conditions and the reversal's characteristics.

4.1. Cold and Dense Versus Hot and Tenuous Plasma Sheet: Relation Between Shielding Evolution and Harang Reversal Formation

4.1.1. Electric Field, Flow, FAC, and Conductance in the Vicinity of the Harang Reversal

[33] As mentioned above, to understand how the plasma sheet number density and temperature affect the overlap of FAC, and thus the Harang reversal, we compare the simulation results between cold and dense plasma sheet case 3 under N IMF conditions (3N) and hot and tenuous plasma sheet case 5 under S IMF conditions (5S).

[34] Figure 5 shows ionospheric FAC projected to the equatorial plane and ionosphere, conductivity in the ionosphere, and pressure in the equatorial plane, for case 3N and 5S, at t = 5 hours. The Harang reversal in case 3N extends from 63° latitude at 2330 MLT to 62° at 0100 MLT, while in case 5S it extends substantially further equatorward and dawnward from the same latitudinal and longitudinal position (63° at 2330 MLT), reaching 58° latitude at 0300 MLT. The westward return flows associated with the Harang reversal in the premidnight sector, just equatorward of the region of high auroral conductance, is seen to be very strong for case 5S, since the electric field in that region is very strong, but weak for case 3N. How the Harang region and the return flows depend on the plasma sheet condition is discussed in section 4.2. It is also clear that the inner edge of Pedersen conductivity, which is actually the electron plasma sheet inner edge, is located at higher latitudes for case 3N than for case 5S.

[35] The latitudinal profiles of ionospheric FAC, Pedersen conductance, and flux tube total content η of 30 eV protons (energy at boundary location: X = 20 R_E at midnight) are compared with the Harang reversal location at 0000 MLT for both cases in Figure 6. In the hot and tenuous plasma sheet case, the Harang reversal is located well equatorward of the peak of upward FAC and of the conductivity peak and very close to the boundary between the downward and upward FAC. However, for the cold and dense case the reversal is located almost at the upward FAC peak and the conductivity peak.

[36] Our interpretation is that, in the 5S case, the shielding of the convection electric field is not effective. Thus low-energy protons penetrate further inward as can be seen by the η latitudinal profile. In fact, they are able to penetrate not only closer to the Earth than the high-energy protons, which are responsible for the upward FAC peak in the overlap region (see section 3.1), but also closer than the high-energy electrons that are responsible for the conductivity peak. This is why the downward current in the overlap region extends to lower latitudes (~58–60°) where conductivity and upward FAC are very weak. Therefore, in the hot and tenuous case, the Harang reversal is located away from the upward FAC and conductivity peaks. The fact that the downward FAC is in the region of weak conductivity also explains the much stronger westward return flow (see discussion about SAPS in section 3.2) in the hot and tenuous case. The electric field perturbations induced by the downward current, being located in the low conductivity region, are very strong.

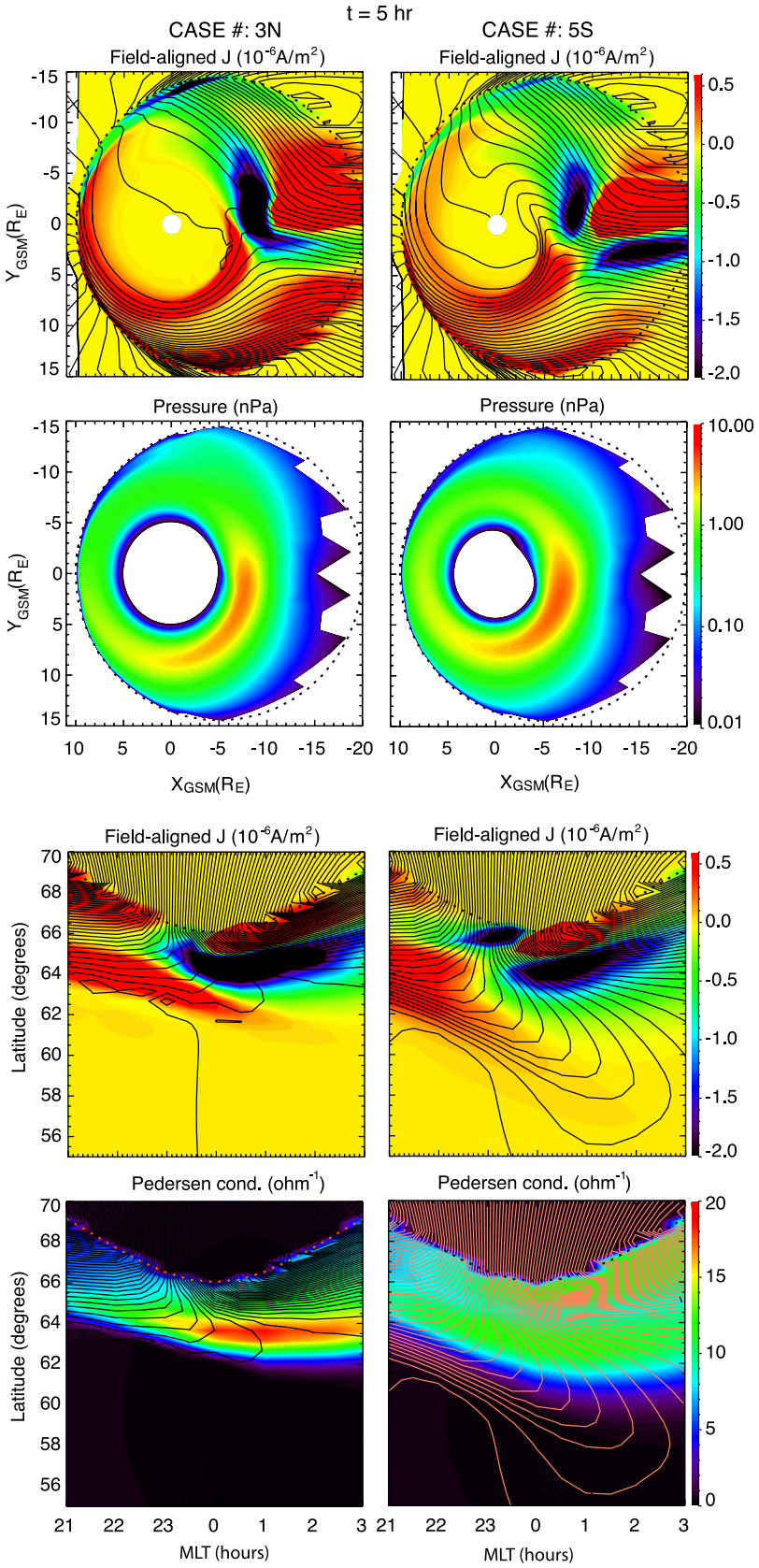

Figure 5. Ionospheric field-aligned currents with equipotentials in the equatorial plane and in the ionosphere, pressure in the equatorial plane, and Pedersen conductivity with equipotentials (1 kV interval) in ionosphere for the cases 3N and 5S.

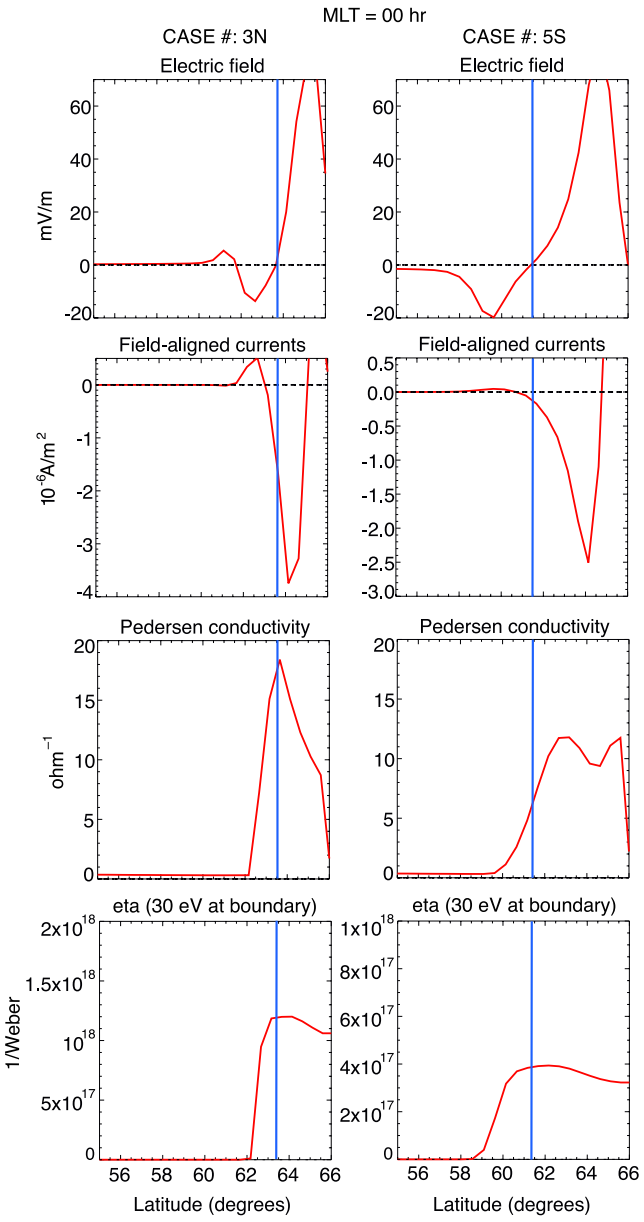

Figure 6. Latitudinal profiles of electric field, field-aligned currents, Pedersen conductance, and flux tube total content η of protons of energy 30 eV at the midnight tail boundary at 0000 MLT for the cases 3N and 5S. The blue line indicates the latitude where the Harang electric field reversal is located.

Therefore, the total electric field is substantially increased, resulting in the enhancement of the **E** $\times$ **B** convection flow in this region.

[37] However, the shielding in 3N case, when the plasma sheet is colder and denser, evolves quickly enough so that the low-energy protons remain further away from the Earth than in the 5S case. Thus the downward FAC of the overlap region remains at higher latitudes closer to the conductivity and upward FAC peaks and so does the Harang reversal.

[38] In Figure 7 we show the latitudinal dependence of the same properties as in Figure 6 but at 0300 MLT. We can see that for the hot and tenuous case there is still a weak electric field reversal attributed to the very small downward current caused by the penetration of the low-energy protons, while for the cold and dense case this penetration, and therefore the overlap of the downward FAC with the upward FAC, is not possible owing to the strong shielding in this region.

[39] Figure 8 shows equipotentials (solid black contours) and the η inner edge for protons (red curve) of the same energy channel (30 eV at the midnight tail boundary) at time t = 0100, 0130, and 0430. These results confirm that, at all MLT, the low-energy protons in the 3N case cannot penetrate as close to the Earth as they do in the 5S one, because the shielding develops quicker in the cold and dense case than in the hot and tenuous one.

4.1.2. Effect of Density and Temperature on Shielding

[40] So far we have shown that penetration of the low-energy protons in the near-Earth region, and therefore the formation of the Harang reversal, strongly depends on the evolution of the shielding of the convection electric field. Since shielding is determined by two major factors, the FAC

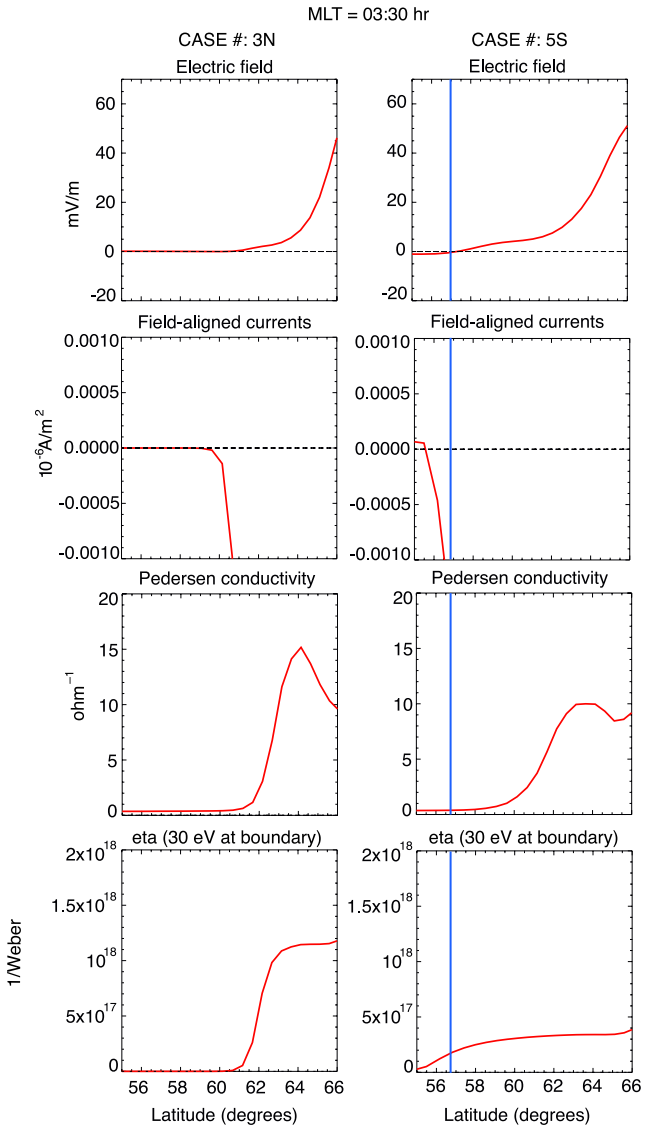

Figure 7. Same as Figure 6 but at 0330 MLT.

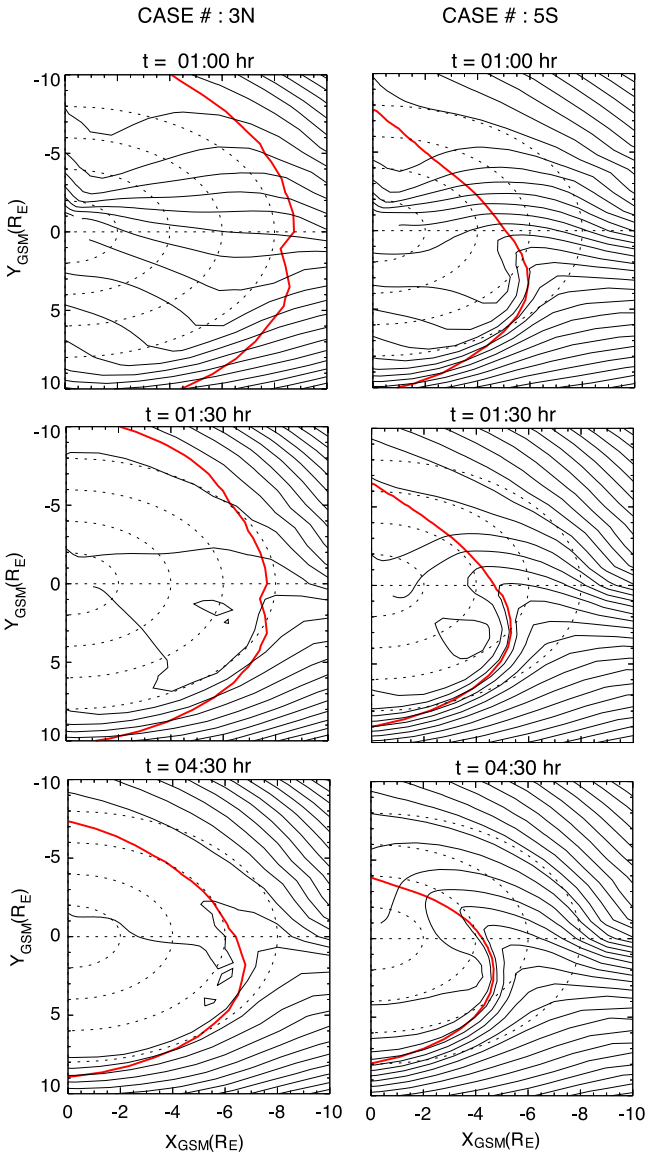

Figure 8. Equipotentials (black solid contours) and η inner edge (red curve) for 30 eV protons at the outer boundary at time t = 0100, 0130, and 0400.

magnitude and the auroral conductivities, the next question is how the plasma sheet state affects these two factors.

[41] As shown in Figure 5, the total FAC strength in the near-Earth region is larger in the cold and dense plasma sheet case than in the hot and tenuous one. This is particularly true for the upward current region, which clearly can be seen to cover a larger region in the cold dense case. Furthermore, the region of enhanced auroral conductance, which is computed from the precipitating electron energy flux estimated from the simulated plasma sheet electron population in these RCM runs, remains restricted to higher latitudes in the cold and dense case, whereas the region is substantially broader and extends to lower latitudes (~60–62°) in the hot and tenuous case. Lower FAC, which require weaker ionospheric currents to maintain current continuity than do higher FAC, and the broader region of higher conductivity means that less electric field perturbation (i.e., less shielding) is required in the hot and tenuous case. The reason for the difference in the conductivity profiles is in part due to the preconditioning, low-energy electrons being able to penetrate closer to the Earth for the hot and tenuous case than for the cold and dense case during the preceding period of weak convection.

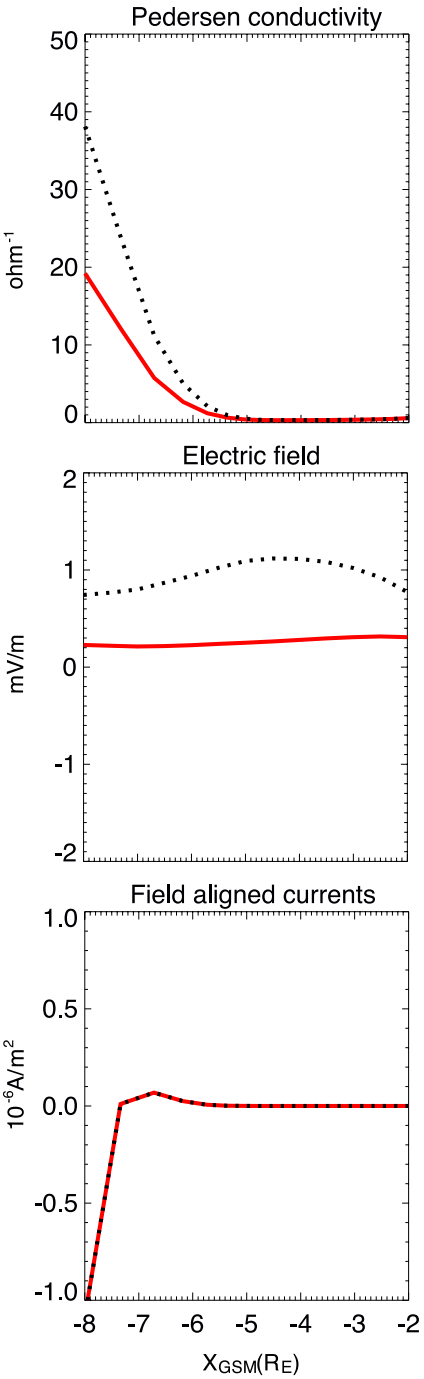

Figure 9. Pedersen conductivity, magnitude of the electric field, and ionospheric field-aligned currents at 0000 MLT and time t = 1 hour versus distance from Earth for the cases 3N (red solid line) and 3N with double conductivity (black dotted line).

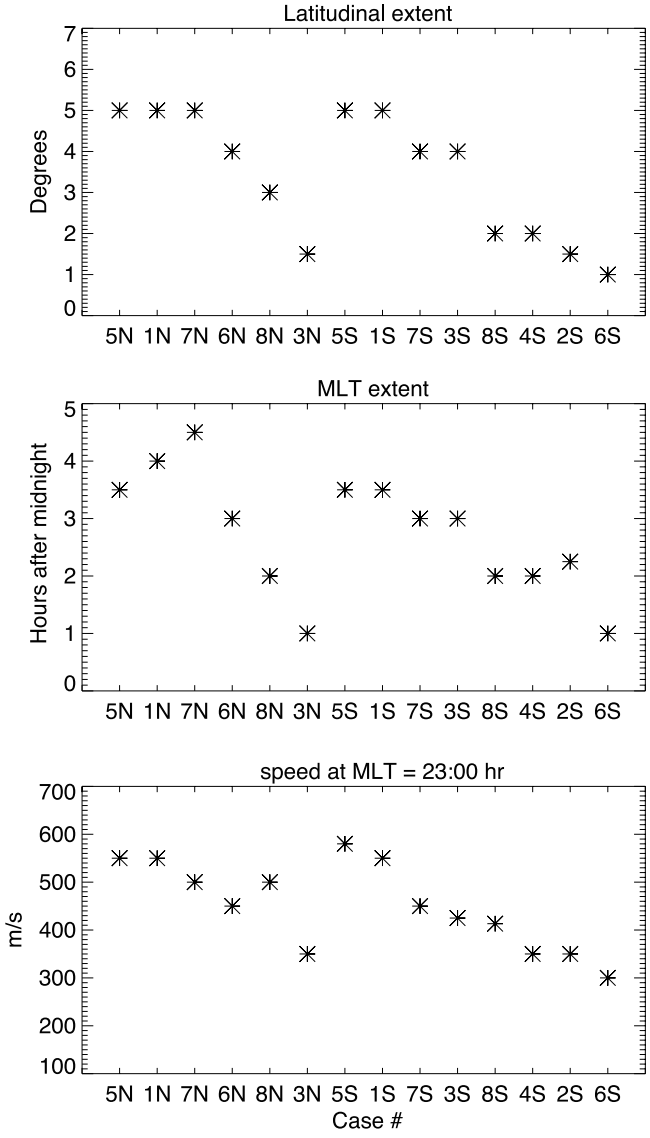

Figure 10. Latitudinal and MLT extent, as well as the magnitude of the peak speed of the westward return flow of the Harang reversal for 14 of our cases.

[42] We verify the point about the contribution of the conductivity to the shielding by doubling only the value of Pedersen conductivity for case 3N at t = 0100. This way, we keep the same magnitude of FAC at this time. Figure 9 shows FAC, conductivity, and magnitude of the electric field at 0000 MLT at t = 0100 versus distance from the Earth for cases 3N (red solid line) and 3N with double conductivity (dotted black line). It can be seen that, although the FACs are the same as expected, since we have not changed anything that would affect the pressure, the near-Earth electric field increases dramatically in the latter case, that is, the shielding is weaker. This is because the electric field perturbations owing to the FAC are of smaller magnitude in response to the much higher conductivity in this region.

[43] *Garner* [2003] also reached the conclusions that shielding is more efficient if the plasma sheet is colder or denser. However, in their numerical experiments with the RCM, they did not include the dependence of the shielding effect on auroral conductivity, since they used an empirical model of the *Kp*-dependent auroral precipitation by *Hardy et al.* [1985] to calculate the auroral conductivities, which does not depend on the plasma sheet condition.

4.2. Harang Reversal Latitudinal Extent, MLT Coverage, and Westward Return Flow

[44] Having determined the parameters that control the shielding of the convection electric field, and therefore the formation of the Harang reversal, we now proceed to our quantitative study of the Harang reversal characteristics.

[45] In Figure 10 we plot the latitudinal and MLT extents, as well as the peak magnitude of the westward return flow at 2300 MLT, of the Harang reversal for 14 of our cases (cases 2 and 4 for NIMF are excluded here because the Harang reversal was almost unidentifiably weak; this is due to the very high plasma sheet density and low electron temperature, and therefore the very strong shielding, for these two cases).

[46] The Harang reversal in cases 1, 5 and 7 for both northward and southward IMF boundary conditions, which are cases of hot and tenuous plasma sheet, has larger latitudinal and longitudinal extent as well as larger peak westward return flow speed than in cases 3, 2, 4, 6 and 8 of colder and denser plasma sheet. These results agree with the physical explanation given in the previous sections about the correlation between plasma sheet conditions, the shielding effect, and the formation of the Harang reversal. In all of the cases, however, the poleward end of the Harang reversal is located around 63° latitude and 2330 MLT. This is because the poleward end of the Harang reversal depends only on the polar cap potential drop and not on the plasma sheet state. Note that observations show that the MLT of the westward end of the Harang reversal depends on the IMF By [*Rodger et al.*, 1984], and the IMF By is known to affect the ionosphere convection pattern and the magnetic field in the magnetosphere. However, the present RCM assumes strict symmetry between the northern and southern ionospheres, and we use IMF By = 0 for the T96 magnetic field model. These restrictions do not allow us to investigate the IMF By effect on the westward-most MLT of the Harang reversal.

5. Conclusions

[47] In this paper we have quantitatively evaluated the physical processes responsible for the Harang reversal and how these processes are affected by the plasma sheet density and temperature. We used the RCM with MLT-dependent plasma sheet boundary conditions that are a function of the interplanetary conditions on the basis of 11 years of Geotail data.

[48] First, we have found that the Harang reversal is a result of an overlap in MLT between the downward and upward region 2 FAC. The upward FAC in the overlapping region is located at higher latitudes and is a result of the pressure peak contributed by the high-energy protons owing to their duskward magnetic drift. The downward FAC, however, is located at lower latitudes and results from the

Table A1. Ranges, Averages, and Standard Deviations of Solar Wind Density, Solar Wind Speed, and Magnitude of Northward or Southward IMF B_z ($|B_{z,\mathrm{IMF}}|$) for the 16 Interplanetary Conditions[a]

Condition	1(N, S) N_{low} V_{low} B_{low}	2(N, S) N_{high} V_{low} B_{low}	3(N, S) N_{low} V_{low} B_{high}	4(N, S) N_{high} V_{low} B_{high}	5(N, S) N_{low} V_{high} B_{low}	6(N, S) N_{high} V_{high} B_{low}	7(N, S) N_{low} V_{high} B_{high}	8(N, S) N_{high} V_{high} B_{high}
N_{sw} (cm^{-3})	[0,6.5]	[6.5,15]	[0,6.5]	[6.5,15]	[0,6.5]	[6.5,15]	[0,6.5]	[6.5,15]
	4.8 ± 1.1	9.7 ± 2.3	4.8 ± 1.2	9.6 ± 2.1	3.8 ± 1.3	8.8 ± 2.0	3.7 ± 1.5	8.9 ± 2.1
V_{sw}	[0,4]	[0,4]	[0,4]	[0,4]	[4,10]	[4,10]	[4,10]	[4,10]
(10^2 km/s)	3.6 ± 0.3	3.5 ± 0.3	3.6 ± 0.2	3.6 ± 0.3	5.1 ± 0.9	4.4 ± 0.4	5.1 ± 0.9	4.5 ± 0.5
$|B_{z,\mathrm{IMF}}|$ (nT)	[0,1.3]	[0,1.3]	[1.3,8]	[1.3,8]	[0,1.3]	[0,1.3]	[1.3,8]	[1.3,8]
	0.6 ± 0.3	0.6 ± 0.4	2.5 ± 1.0	2.8 ± 1.5	0.6 ± 0.4	0.6 ± 0.4	2.5 ± 1.1	2.9 ± 1.4

[a]Values inside brackets represent ranges. Abbreviations are as follows: N_{sw}, solar wind density; V_{sw}, solar wind speed; N, northward; S, southward.

pressure peak caused by the plasma sheet electrons and low-energy plasma sheet protons, which penetrate closer to the Earth at the midnight and postmidnight MLT than do the high-energy protons. The earthward penetration of the low-energy protons into the near-Earth region, which is crucial for the formation of the Harang reversal, strongly depends on the shielding of the convection electric field.

[49] We found that the shielding is more efficient for a colder and denser plasma sheet, which is often found in the cases of higher solar wind density, than for a hotter and more tenuous plasma sheet found in the cases of lower solar wind density. A combination of higher pressure, and therefore stronger FAC in the near-Earth region, and lower auroral conductance at low latitudes in the colder and denser plasma sheet, results in enhanced shielding of the penetration electric field. However, in the hot and tenuous case, the pressure and FAC magnitudes in the inner magnetosphere are lower and the conductivity is higher, therefore the shielding is weaker.

[50] The above arguments lead us to the conclusion that in hot and tenuous plasma sheet conditions, when the shielding of the convection electric field is not efficient, the low-energy protons get much closer to the Earth than the high-energy protons and the high-energy electrons. This way, the downward FAC in the overlapping region is located at lower latitudes, further equatorward from the upward FAC peak and the conductivity peak, and extends further toward postmidnight MLT. The location of the downward current in the region of weak conductivity also explains the much stronger SAPS for a hot and tenuous plasma sheet, since the electric field perturbations induced by the downward FAC are very strong, causing a substantial increase in the total electric field, thus an enhancement of the $\mathbf{E} \times \mathbf{B}$ convection flow in this region.

[51] Therefore, in the cases of lower plasma sheet number density, the Harang reversal has larger latitudinal and MLT extent and stronger westward return flows (SAPS), than in the cases with higher plasma sheet number density.

Appendix A

[52] To establish the plasma boundary conditions for the RCM we fit the Geotail particle distribution of the 16 different

Table A2. Values of κ for Hot Population, Number Density, and Temperature for Cold and Hot Population of Electrons and Protons for the Eight Cases Under N IMF Conditions[a]

	κ_h	N_h (cm^{-3})	T_h (keV)	N_c (cm^{-3})	T_c (keV)
			N IMF 1		
e	10, 6, 5	0.2, 0.05, 0.14	0.8, 0.8, 0.8	0.15, 0.06, 0.14	0.1, 0.1, 0.1
p	10, 5, 9.5	0.2, 0.06, 0.14	2.5, 4, 2,	0.15, 0.05, 0.6	1, 5, 2
			N IMF 2		
e	8, 7, 6	0.2, 0.15, 0.3	0.8, 0.8, 0.8	0.5, 0.1, 0.8	0.08, 0.12, 0.07
p	10.5, 5, 10.7	0.4, 0.15, 0.5	4, 4, 3	0.3, 0.1, 0.6	1, 3, 1
			N IMF 3		
e	10, 10.5, 8	0.1, 0.06, 0.1	0.6, 0.5, 0.7	0.5, 0.14, 0.7	0.05, 0.1, 0.07
p	10.5, 10.8, 7	0.15, 1, 0.3	2.5, 3.5, 5	0.45, 0.1, 0.5	0.6, 1.5, 1
			N IMF 4		
e	10.5, 8, 9.5	0.15, 0.04, 0.13	0.5, 1.2, 0.7	1, 0.3, 1.07	0.07, 0.07, 0.07
p	10.5, 10, 11	0.4, 0.12, 0.3	3, 4, 1.5	0.75, 0.22, 0.9	0.3, 1.3, 0.4
			N IMF 5		
e	9, 6, 3	0.1, 0.045, 0.2	1, 1, 1	0.15, 0.05, 0.25	0.15, 0.15, 0.15
p	7, 4, 10.5	0.1, 0.045, 0.2	6, 5, 4	0.15, 0.05, 0.25	1, 3, 1
			N IMF 6		
e	10.5, 8, 4	0.2, 0.1, 0.15	1, 1, 1	0.2, 0.03, 0.4	0.1, 0.1, 0.1
p	6, 4, 10.5	0.2, 0.06, 0.15	6, 6, 3	0.2, 0.07, 0.4	1, 4, 1
			N IMF 7		
e	10.3, 6, 4	0.05, 0.03, 0.1	0.8, 0.8, 0.8	0.3, 0.07, 0.4	0.07, 0.15, 0.08
p	10, 7, 11	0.1, 0.06, 0.2	5, 4, 3	0.25, 0.04, 0.3	1, 1.5, 2
			N IMF 8		
e	10.3, 6, 4	0.05, 0.1, 0.3	0.6, 0.8, 0.8	0.7, 0.08, 0.6	0.06, 0.12, 0.07
p	10.5, 8, 10.8	0.15, 0.1, 0.4	4, 4, 4	0.6, 0.08, 0.6	0.6, 4, 1

[a]The first number is the value at dusk, the second at midnight and third at dawn. The values for the other nightside MLT are obtained by linear interpolation between these values. Abbreviations are as follows: c, cold; h, hot; e, electrons; p, protons.

Table A3. Same as Table A2 but Under S IMF Conditions

	κ_h	N_h (cm^{-3})	T_h (keV)	N_c (cm^{-3})	T_c (keV)
			S IMF 1		
e	8, 7, 6	0.1, 0.08, 0.15	0.9, 0.9, 0.9	0.1, 0.02, 0.2	0.1, 0.09, 0.08
p	8, 6, 10.5	0.15, 0.05, 0.15	3, 5, 3	0.05, 0.05, 0.2	1, 4, 1
			S IMF 2		
e	9, 6, 7	0.2, 0.12, 0.3	0.8, 0.8, 0.8	0.2, 0.05, 0.6	0.1, 0.09, 0.07
p	7, 4, 10.5	0.2, 0.1, 0.3	4, 4, 4	0.2, 0.07, 0.6	0.5, 5, 0.4
			S IMF 3		
e	7, 9, 3	0.15, 0.1, 0.18	1, 1, 1	0.04, 0.02, 0.08	0.05, 0.06, 0.08
p	6, 10, 4	0.18, 0.07, 0.2	4, 5, 4	0.01, 0.05, 0.06	1.5, 3, 1
			S IMF 4		
e	8, 6, 7	0.1, 0.13, 0.3	1, 1, 1	0.07, 0.03, 0.1	0.09, 0.09, 0.09
p	5, 4, 11	0.15, 0.1, 0.3	6, 5, 4	0.12, 0.06, 0.1	3, 4, 3
			S IMF 5		
e	7, 6, 4	0.1, 0.05, 0.1	1.2, 1.2, 1.2	0.1, 0.02, 0.3	0.15, 0.1, 0.08
p	7, 4, 12	0.1, 0.05, 0.2	8, 6, 4	0.1, 0.02, 0.2	2, 4, 0.5
			S IMF 6		
e	8, 6, 8	0.15, 0.15, 0.15	1, 1, 1	0.2, 0.05, 0.25	0.1, 0.1, 0.1
p	12, 4, 8	0.15, 0.1, 0.2	6, 9, 4	0.2, 0.1, 0.2	2, 1, 4
			S IMF 7		
e	8, 6, 5	0.06, 0.08, 0.2	1.5, 1.5, 1.5	0.06, 0.02, 0.2	0.15, 0.1, 0.15
p	3, 8, 4	0.06, 0.08, 0.15	8, 8, 8	0.06, 0.02, 0.025	0.4, 1.5, 2
			S IMF 8		
e	5, 5, 5	0.2, 0.12, 0.2	1, 1, 1	0.1, 0.03, 0.3	0.1, 0.15, 0.09
p	6, 4, 12	0.2, 0.1, 0.2	5, 7, 5	0.1, 0.05, 0.3	2, 3, 1

interplanetary conditions (listed in Table A1) with a two-component kappa distribution.

$$f = N_c\left(\frac{m}{2\pi\kappa_c E_{0,c}}\right)^{3/2}\frac{\Gamma(\kappa_c+1)}{\Gamma(\kappa_c-1/2)}\left[1+\frac{E}{\kappa_c E_{0,c}}\right]^{-\kappa_c-1} + N_h\left(\frac{m}{2\pi\kappa_h E_{0,h}}\right)^{3/2}\frac{\Gamma(\kappa_h+1)}{\Gamma(\kappa_h-1/2)}\left[1+\frac{E}{\kappa_h E_{0,h}}\right]^{-\kappa_h-1} \quad \text{(A1)}$$

N, κ, and E_0 are free parameters in the fitting, and their values are listed in Table A2 for northward IMF and Table A3 for southward IMF. The κ values for the cold population for both electrons and protons are omitted from Tables A2 and A3 since they have a constant value of $\kappa = 4$.

[53] **Acknowledgments.** The work by M. Gkioulidou has been supported by NASA grant NNX07AF66G and NSF grant ATM-0819864. The work by C.-P. Wang and L. R. Lyons has been supported by NASA grants NNX07AF66G, NNX07AG42G, and NNX08A135G, and NSF grant ATM-0819864. The work by R. A. Wolf has been supported by the Heliospheric Theory Program under grant NNX08AI55G.

[54] Amitava Bhattacharjee thanks Mike Kosch and Raymond Greenwald for their assistance in evaluating this paper.

References

Anderson, P. C., R. A. Heelis, and W. B. Hanson (1991), The ionospheric signatures of rapid subauroral ion drifts, *J. Geophys. Res.*, *96*, 5785–5792, doi:10.1029/90JA02651.

Bristow, W. A., and P. Jensen (2007), A superposed epoch study of SuperDARN convection observations during substorms, *J. Geophys. Res.*, *112*, A06232, doi:10.1029/2006JA012049.

Erickson, G. M., R. W. Spiro, and R. A. Wolf (1991), The physics of the Harang discontinuity, *J. Geophys. Res.*, *96*, 1633–1645, doi:10.1029/90JA02344.

Foster, J. C., and W. J. Burke (2002), SAPS: A new categorization for sub-auroral electric fields, *Eos Trans. AGU*, *83*(36), 393, doi:10.1029/2002EO000289.

Garner, T. W. (2003), Numerical experiments on the inner magnetospheric electric field, *J. Geophys. Res.*, *108*(A10), 1373, doi:10.1029/2003JA010039.

Harang, L. (1946), The mean field of disturbance of polar geomagnetic, *Terr. Magn. Atmos. Electr.*, *51*(3), 353–380, doi:10.1029/TE051i003p00353.

Hardy, D., M. Gussenhoven, and E. Holeman (1985), A statistical model of auroral electron precipitation, *J. Geophys. Res.*, *90*, 4229–4248, doi:10.1029/JA090iA05p04229.

Harel, M., R. A. Wolf, P. H. Reiff, R. W. Spiro, W. J. Burke, F. J. Rich, and M. Smiddy (1981a), Quantitative simulation of a magnetospheric substorm, 1, model logic and overview, *J. Geophys. Res.*, *86*, 2217–2241, doi:10.1029/JA086iA04p02217.

Harel, M., R. A. Wolf, P. H. Reiff, R. W. Spiro, W. J. Burke, F. J. Rich, and M. Smiddy (1981b), Quantitative simulation of a magnetospheric substorm, 2, comparison with observations, *J. Geophys. Res.*, *86*, 2242–2260, doi:10.1029/JA086iA04p02242.

Lyons, L. R., C.-P. Wang, and T. Nagai (2003), Substorm onset by plasma sheet divergence, *J. Geophys. Res.*, *108*(A12), 1427, doi:10.1029/2003JA010178.

Nakamura, M., G. Paschmann, W. Baumjohann, and N. Sckopke (1991), Ions distributions and flows near the neutral sheet, *J. Geophys. Res.*, *96*, 5631–5649, doi:10.1029/90JA02495.

Nielsen, E., and R. A. Greenwald (1979), Electron flow and visual aurora at the Harang discontinuity, *J. Geophys. Res.*, *84*, 4189–4199, doi:10.1029/JA084iA08p04189.

Robinson, R. M., R. R. Vondrak, K. Miller, T. Dabbs, and D. Hardy (1987), On calculating ionospheric conductances from the flux and energy of precipitating electrons, *J. Geophys. Res.*, *92*, 2565–2569, doi:10.1029/JA092iA03p02565.

Rodger, A. S., S. W. H. Cowley, M. J. Brown, M. Pinnock, and D. A. Simmons (1984), Dawn-dusk (y) component of the interplanetary magnetic field and the local time of the Harang discontinuity, *Planet. Space Sci.*, *32*(8), 1021–1027, doi:10.1016/0032-0633(84)90058-8.

Southwood, D. J., and R. A. Wolf (1978), An assessment of the role of precipitation in magnetospheric convection, *J. Geophys. Res.*, *83*, 5227–5232, doi:10.1029/JA083iA11p05227.

Stiles, G. S., E. W. Hones Jr., S. J. Bame, and J. R. Asbridge (1978), Plasma sheet pressure anisotropies, *J. Geophys. Res.*, *83*, 3166–3172, doi:10.1029/JA083iA07p03166.

Toffoletto, F., S. Sazykin, R. Spiro, and R. Wolf (2003), Inner magnetospheric modeling with the Rice convection model, *Space Sci. Rev.*, *107*, 175–196, doi:10.1023/A:1025532008047.

Tsyganenko, N. A. (1995), Modeling the Earth's magnetospheric magnetic field confined within a realistic magnetopause, *J. Geophys. Res.*, *100*, 5599–5612, doi:10.1029/94JA03193.

Tsyganenko, N. A. (1996), Effects of the solar wind conditions on the global magnetospheric configuration as deduced from data-based field models, *Eur. Space Agency Spec. Publ.*, *389*, 181–185.

Vasyliunas, V. M. (1970), Mathematical models of magnetospheric convections and its coupling to the ionosphere, in *Particles and Fields in the Magnetosphere*, edited by B. M. McCormac, pp. 60–71, D. Reidel, Norwell, Mass.

Wang, C.-P., L. R. Lyons, T. Nagai, J. M. Weygand, and R. W. McEntire (2007), Sources, transport, and distributions of plasma sheet ions and electrons and dependences on interplanetary parameters under northward interplanetary magnetic field, *J. Geophys. Res.*, *112*, A10224, doi:10.1029/2007JA012522.

Wolf, R. A. (1983), The quasi-static (slow-flow) region of the magnetosphere, in *Solar Terrestrial Physics*, edited by R. L. Carovillano and J. M. Forbes, pp. 303–368, D. Reidel, Norwell, Mass.

Zou, S., L. R. Lyons, C.-P. Wang, A. Boudouridis, J. Ruohoniemi, M. Anderson, P. C. Dyson, and P. L. Devlin (2009), On the coupling between the Harang reversal evolution and substorm dynamics: A synthesis of SuperDARN, DMSP, and IMAGE observations, *J. Geophys. Res.*, *114*, A01205, doi:10.1029/2008JA013449.

M. Gkioulidou, L. R. Lyons, and C.-P. Wang, Department of Atmospheric and Oceanic Sciences, University of California, MS-71, 405 Hilgard Avenue, Los Angeles, CA 90095-1565, USA. (mgioul@atmos.ucla.edu)

R. A. Wolf, Physics and Astronomy Department, Rice University, MS 108, 202 Herman Brown Hall, Houston, TX 77005-0000, USA.